CHEMIJA. 2020. Vol. 31. No. 1. P. 11–24

Surfactant-assisted microwave synthesis of carbon supported MnO_2 nanocomposites and their application for electrochemical supercapacitors

Jolita Jablonskienė*,

Dijana Šimkūnaitė,

Jūratė Vaičiūnienė,

Algirdas Selskis,

Audrius Drabavičius,

Vitalija Jasulaitienė,

Loreta Tamašauskaitė-Tamašiūnaitė,

Eugenijus Norkus

Center for Physical Sciences and Technology,
3 Saulėtekio Avenue,
10257 Vilnius, Lithuania

MnO_2/C nanocomposites have been prepared using a simple one-step microwave heating method by applying different concentrations of cationic surfactant – cetyl trimethylammonium bromide (CTAB). The morphology and composition of the prepared MnO_2/C nanocomposites have been investigated using X-ray photoelectron spectroscopy (XPS), field-emission scanning electron microscopy (FE-SEM), transmission electron microscopy (TEM), and inductively coupled plasma optical emission spectroscopy (ICP-OES). The electrochemical performance of the prepared nanocomposites has been analysed using cyclic voltammetry. It was found that a high specific capacitance (C_s) of 742 F g^{-1} at a scan rate of 10 mV s^{-1} in a 1 M Na_2SO_4 solution has been obtained for the MnO_2/C nanocomposite that has the mass loading of 0.140 mg cm^{-2} and has been synthesized in the absence of CTAB. Meanwhile, the application of CTAB allowed the increase in the mass loading of MnO_2 in the nanocomposites. In the presence of CTAB, the highest value of 654 F g^{-1} at a scan rate of 10 mV s^{-1} has been obtained for MnO_2/C that has the mass loading of 0.570 mg cm^{-2}. This result confirmed a good performance of the prepared MnO_2/C nanocomposites as the electrode material for supercapacitors.

Keywords: MnO_2/C nanocomposites, microwave synthesis, CTAB, specific capacitance, supercapacitors

INTRODUCTION

Increasing demand for renewable and sustainable energy sources extremely necessitates the development of high-performance, environment-friendly, flexible, light and inexpensive energy storage and conversion devices [1–5]. To meet those requirements fuel cells, batteries and supercapacitors (SCs) are under serious consideration for electrochemical efficient and clean energy storage/conversion strategy [6–9]. Among them, SCs are widely viewed as potential candidates of next-generation energy storage devices [10, 11]. From the point view of power and energy density characteristics they are much regarded for considerably larger power densities than batteries or fuel cells and larger energy densities than conventional capacitors [1, 12]. The main advantages of SCs over fuel cells and batteries are referred to their long charging/discharging cycles and a wide

* Corresponding author. Email: jolita.jablonskiene@ftmc.lt

operating temperature range [13]. Moreover, they cover a large-scale of possible applications ranging from consumer electronic or portable devices like mobile phones, computers, memory back-up systems to hybrid electric vehicles or even large industrial machinery, for defence and military or space equipment, as well as for medical, industrial needs and many more [1, 14–17].

Depending on the charge-storage mechanism two types of SCs are denoted: nonfaradaic – electric double-layer capacitors (EDLCs) or – faradaic – pseudocapacitors. In EDLCs charge is stored by ions adsorption–desorption process mainly on high-surface area carbon-based materials. Meanwhile, in pseudocapacitors charge is stored via fast and reversible redox reactions on the surface or near the surface of transition metal oxides (e.g. IrO_2, RuO_2, Fe_3O_4, MnO_2, NiO, V_2O_5, Co_3O_4, etc.), conducting polymers (e.g. polyaniline, polythiophene, polypyrrole, polyvinyl alcohol, poly-phenylene-vinylene, etc.), transition metal dichalcogenides (sulphides, selenides), etc. [1]. Coupling both Faradaic and non-Faradaic processes inherent to pseudocapacitors or EDLCs, respectively, allowed developing hybrid SCs systems with superior characteristics, e.g. significantly higher power and energy densities, compared to those values obtained at each system separately [14, 18]. Typically, pseudocapacitors have a considerably improved specific capacitance compared with that of carbon-based EDLCs [19, 20]. However, their electrochemical performance is largely limited due to the degradation of electrode material.

Among the reported transition metal oxide materials for pseudocapacitors, RuO_2 has drawn the greatest attention for its extremely high theoretical specific (C_s) value, which is greater than 1300 F g^{-1} and has a good thermal stability and electrochemical reversibility, a high rate capability, a wide potential window, and a long life-cycle [14, 18, 21]. However, a relatively high cost, toxicity and limited environmental distribution of RuO_2 restrict its large-scale commercial application in SCs. On the contrary, MnO_2, as a kind of low price, abundant, environment-friendly material that has various morphologies and exceptionally high theoretical specific capacitance (C_s) close to 1370 F g^{-1}, is a perfect replacement for the state-of-the-art RuO_2-based pseudocapacitors [12, 22]. Regardless of the superb characteristics, the main drawback for its (MnO_2) widespread application is poor electrical conductivity (10^{-5} – 10^{-6} S cm^{-1}). Moreover, the achieved capacitance value remains much smaller compared to that theoretically predicted and decreases rapidly with the increase in the MnO_2 mass loading [23]. Furthermore, only an ultrathin MnO_2 deposit allows achieving better electrochemical performance [23]. One possible way to increase C_s is applying nanostructured MnO_2-based electrodes that have a high specific surface area, such as mesoporous MnO_2 nanotubes [24], nanowires [25–28], nanosheets [24, 29], thin films [30] and flower-like structures [31]. Another way to improve C_s of MnO_2-based electrodes is deposition of thin films of these materials on highly conductive surfaces. Recently, carbon-based materials with an excellent conductivity and ultrastability (representing EDLCs performance) have been hybridized with MnO_2 (the representing pseudocapacitive performance). This allowed overcoming the limitations of each material by making full use of their advantages due to the synergistic effects between those two types of SCs [32–34].

However, in order to meet the requirements for commercial applications of the SCs, high mass loadings are essential. Usually, a good electrochemical performance is related with the low mass loading (typically less than 0.3 mg cm^{-2}). In order to achieve a high power and energy performance of the capacitor device in practical application, a large mass loading of active material is needed [23]. Recently, highly loaded manganese oxide with a high mass loading of 7.02 mg cm^{-2} was shown to exhibit an excellent rate capability due to the dual-tuning effect. Meanwhile, an excellent C_s of 161.2 F g^{-1} and areal capacitance (C_{areal}) of 1.13 F cm^{-2} at a high current density of 20 mA cm^{-2}, comparable to that delivered by the low mass loading electrode at the same current density, have been obtained [35]. In Ref. [36] a nanostructured porous MnO_2 film on a Ni foam substrate was fabricated via a CV electrodeposition route with a high mass loading from 6 to 18 mg cm^{-2}. It delivered the maximum C_{areal} of 2.79 F cm^{-2} at a current density of 2 mA cm^{-2}. The hybrid MnO_2/3D-PC of nanostructured MnO_2 and 3D-porous carbon (PC) have been fabricated [37]. Such porous 3D-PC structures allowed achieving a large MnO_2 mass loading of

11.5 mg cm^{-2}, which resulted in a high areal capacitance of 2.77 F cm^{-2} at a scan rate of 1 mV s^{-1}. C_s of 416 F g^{-1} was obtained based on the mass loading of 2.52 mg cm^{-2} at a scan rate of 1 mV s^{-1} [37].

Notwithstanding, the relatively low mass loading of MnO_2 and low volumetric or gravimetric energy density remain a problem yet. It is still a challenge for synthesizing the electrode materials for SCs with both high mass loading and excellent electrochemical properties. Bearing in mind that the electrochemical performance of SCs is to a large extent determined by the properties of electrode materials, considerable efforts are aimed at improving the properties of MnO_2 electrodes. In order to achieve those requirements, various surfactants including cetyl trimethylammonium bromide (CTAB) for adjusting the desired structure and morphology growth of electrode material are frequently applied. This agent is known to enhance the dispersion of the MnO_2 particles, increase the specific surface area and improve the pore structure of particles [38, 39]. Different methods in the presence of CTAB like liquid co-precipitation [38, 39], direct cyclic voltammetry electrodeposition [40] or galvanostatic cathodic electrosynthesis [41] have been applied for the synthesis of MnO_2 electrode material. In all those cases, the obtained C_s values have been sufficiently high and delivered increased C_s values when compared to those obtained at the parent MnO_2 electrode material prepared without surfactant CTAB. Various preparing methods of electrode material for SCs allow obtaining MnO_2 with a different structure and morphology by controlling the reaction conditions and parameters. However, most of the reported methods are tedious and expensive, employ templates or even use noble metals.

There are some few works showing a clear effect of microwave-assisted synthesis on the surface morphology and other physicochemical properties of α-MnO_2 without applying any surfactants [42–46]. To our knowledge, the application of CTAB in microwave-assisted synthesis for fabrication of fine MnO_2 nanoparticles has not been reported until now. In this study, we prepared carbon supported MnO_2 nanoparticle composites using the CTAB as an additive by the simple, facile and reliable one-step microwave heating method. The crystal structure, morphology and composition of MnO_2/C nanocomposites were systematically analysed using X-ray diffraction (XRD), X-ray photoelectron spectroscopy (XPS), field emission scanning electron microscopy (FE-SEM) and transmission electron microscopy (TEM). The electrochemical performances of the prepared nanocomposites were analysed using cyclic voltammetry (CV).

EXPERIMENTAL

Chemicals

$KMnO_4$, CTAB, Na_2SO_4, graphite powder (99.9995%), polyvinylidene fluoride (PVDF) and N-methyl-2-pyrrolidinone (NMP) were purchased from Sigma-Aldrich Supply and used as received without further purification. Ultra-pure water with the resistivity of 18.2 MΩ cm^{-1} was used to prepare all the solutions. All the reagents used were of analytical grade.

Fabrication of MnO_2/C nanocomposites

MnO_2/C nanocomposites were prepared by microwave-assisted heating without CTAB or using CTAB as an additive. In a typical experiment, 0.1 g of graphite was dispersed in ultra-pure water and sonicated for 30 min. Then, 0.2 or 2 g of $KMnO_4$ was added into the solution and sonicated for 10 min. The total volume of prepared reaction mixtures was 20 ml. The obtained reaction mixtures were put into a microwave reactor Monowave 300 (Anton Paar). The synthesis of MnO_2/C was carried out at 150°C temperature for 5 min. Then, the obtained precipitates were filtered out, washed with ultra-pure water and dried in a vacuum oven at 80°C temperature for 4 h. The synthesized MnO_2/C nanocomposites were denoted as MnO_2/C-1 and MnO_2/C-2. In general, the reaction between the carbon atoms and $KMnO_4$ can be described as the following reaction (Eq. 1) [12, 13]:

$$4\,KMnO_4 + 3\,C + H_2O \rightarrow 4\,MnO_2 + \\ + K_2CO_3 + 2\,KHCO_3. \quad (1)$$

The synthesis of MnO_2/C nanocomposites using CTAB as an additive was carried out under the same conditions. The total volume of the prepared reaction mixtures was 20 ml. The amount of

$KMnO_4$ was 0.2 g and that of graphite was 0.1 g, whereas different amounts of the 0.03 M CTAB solution were added to the mixture – 0.05, 0.5, 1 and 5 ml. The synthesized nanocomposites were denoted as $MnO_2/C_{CTAB\text{-}0.05}$, $MnO_2/C_{CTAB\text{-}0.5}$, $MnO_2/C_{CTAB\text{-}1}$ and $MnO_2/C_{CTAB\text{-}5}$, respectively.

Physical characterization

A shape and size of catalyst particles were examined using a transmission electron microscope Tecnai G2 F20 X-TWIN equipped with an EDX spectrometer with an r-TEM detector. For microscopic examinations, 10 mg of the sample was first sonicated in 1 ml of ethanol for 1 h and then deposited on the Ni grid covered with a continuous carbon film.

Elemental analysis of deposits was studied by XPS using an ESCALAB MK II spectrometer (VG Scientific, UK) equipped with a Mg Kα X-ray radiation source (1253.6 eV) operated at 300 W and at the fixed pass energy of 20 eV. The pressure of 1.33×10^{-6} Pa was kept in the UHV analysis chamber. The XPS spectra were recorded for Mn 2p, O 1s and C 1s.

The Mn loading in the prepared samples was estimated from ICP-OES measurements. The ICP optical emission spectra were recorded using an ICP optical emission spectrometer Optima 7000DV (Perkin Elmer).

Preparation of electrodes and electrochemical measurements

All electrochemical measurements were performed with a Zennium electrochemical workstation (ZAHNER-Elektrik GmbH & Co.KG). The three-electrode electrochemical cell was used. The prepared MnO_2/C nanocomposites coated on the glassy carbon electrode (GCE) with a geometric surface area of 0.07 cm^2 were employed as a working electrode, a Pt plate as a counter electrode, and an Ag/AgCl/KCl electrode was used as a reference. The electrode potential is quoted versus the standard hydrogen electrode (SHE). Steady state linear sweep voltammograms were recorded in a 1 M Na_2SO_4 solution at different scan rates between 10 and 200 mV s^{-1} at ambient temperature. The measuring potential range was from 0.05 to 1.1 V. All solutions were deaerated by argon for 15 min prior to measurements.

The working electrodes were prepared as follows: the 10 mg of the active material (MnO_2/C) were dispersed ultrasonically in 0.1 ml of 2% of PVDF in an NMP solution for 1 h. Then, 5 μL of the obtained slurry was pipetted onto the polished surface of GCE and dried in an oven at 80°C temperature for 2 h.

The specific capacitance C_S (F g^{-1}) of the electrode material was calculated from the CV test according to the following equation (2) [41]:

$$C_s = \frac{1}{m \cdot v \cdot \Delta V} \int i dv . \quad (2)$$

Here C_s, m, v, ΔV and i denote the specific capacitance (F g^{-1}), the mass of the composite film (g), the scan rate of potential (V s^{-1}), the range of scan potential (V) and the response current (A), respectively.

RESULTS AND DISCUSSION

SEM analyses have been performed to probe the surface structural identities of MnO_2/C samples prepared by the microwave-assisted heating method. Figure 1a, b shows the typical images of MnO_2/C-1, which was prepared in the absence of CTAB, under different magnifications. As seen from the image of the MnO_2/C-1 nanocomposite in Fig. 1a, sparsely distributed spherical (nanostructures) nanoparticles of ca. 10–20 nm in size on the surface that have a large number of gully folds are observed. This result indicates the spherical grain morphology of MnO_2 spread over the whole surface with a porous structure. Meanwhile, in the high-magnification SEM image the presence of a characteristic thin nanosheet structure with 2–3 nm in thickness in the background of larger nanostructures of ca. 10–20 nm in size is discerned (Fig. 1b).

The SEM images of the $MnO_2/C_{CTAB\text{-}5}$ nanocomposite are given in Fig. 1c, d under different magnifications. The addition of surfactant CTAB can reduce the agglomeration of MnO_2 particles and make their distribution more even. This is mainly related to the formation process of the MnO_2 crystal nucleus. The $MnO_2/C_{CTAB\text{-}5}$ sample is composed of a significantly larger amount (of ca. 10 times) of aggregated nanoparticles ranging from ca. 100 to 200 nm in diameter (Fig. 1c). They consist of curled, distorted and thin nanosheets as depicted in Fig. 1d. The porous structure was also maintained in this case.

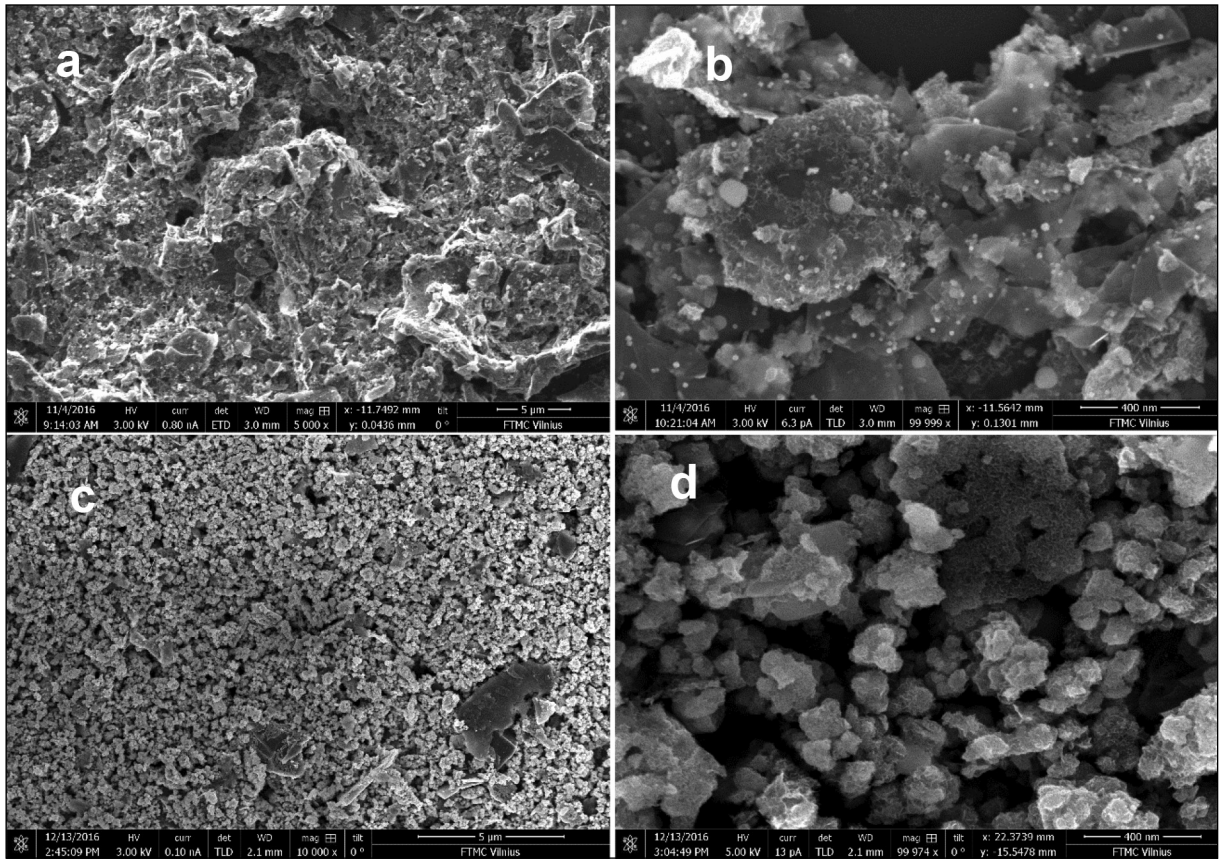

Fig. 1. SEM images of MnO_2/C-1 (a, b) and MnO_2/C_{CTAB-5} (c, d) under different magnifications

It has been determined that the applying of CTAB as an additive for the synthesis of MnO_2/C nanocomposites allows the obtaining of nanocomposites that have higher Mn mass loading as compared with the nanocomposites that were synthesized without CTAB as an additive. The summarized data of EDX and ICP-OES analyses of the prepared nanocomposites are given in Table 1. It is seen that depending on the amount of CTAB used in the synthesis of nanocomposites, the MnO_2/C nanocomposites that have ca. 1.5–11.3 times higher Mn loadings were synthesized as compared with the nanocomposites synthesized without CTAB (Table 1).

MnO_2/C-1 and MnO_2/C_{CTAB-5} samples were further characterized by TEM analysis. TEM images also confirm the fibrous morphologies of both samples with the more expressed one for the MnO_2/C_{CTAB-5} sample (Fig. 2) and show an excellent agreement with the results obtained by SEM. It was found that the size of MnO_2 nanoparticles is ca. 13–18 nm in the prepared MnO_2/C-1 sample (Fig. 2a, b). No large MnO_2 nanoparticles are present within the prepared sample, indicating negligible particles aggregation.

Table 1. **The atomic surface composition of MnO_2/C samples, which were prepared without CTAB and with CTAB as an additive, determined by EDX analysis. Mn loading in the nanocomposites was determined by ICP-OES analysis**

Sample	Mn loading, mg_{Mn} cm^{-2}
MnO_2/C-1	0.140
MnO_2/C-2	0.239
$MnO_2/C_{CTAB-0.05}$	0.207
$MnO_2/C_{CTAB-0.5}$	0.570
MnO_2/C_{CTAB-1}	0.485
MnO_2/C_{CTAB-5}	1.583

The hollow structure of sample C may be the reason of its high specific capacitance.

In order to get information on the manganese oxidation states at the surface of MnO_2/C samples, XPS spectra of Mn 2p, O 1s and C 1s were recorded for MnO_2/C-1, MnO_2/C_{CTAB-1} and MnO_2/C_{CTAB-5} samples and are shown in Figs. 3 and 4. The summarized data are given in Table 2. The C 1s signal, as well as Mn 2p and O 1s peaks are clearly observed

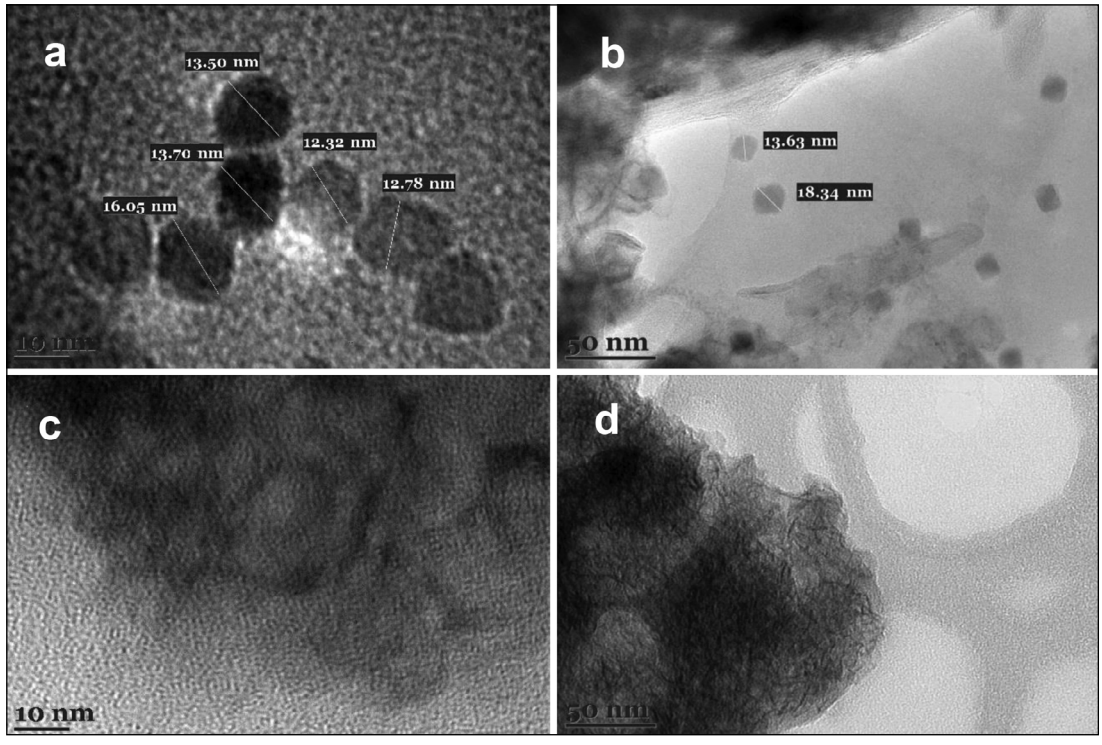

Fig. 2. TEM images of MnO_2/C-1 (a, b) and $MnO_2/C_{CTAB\text{-}5}$ (c, d) nanocomposites

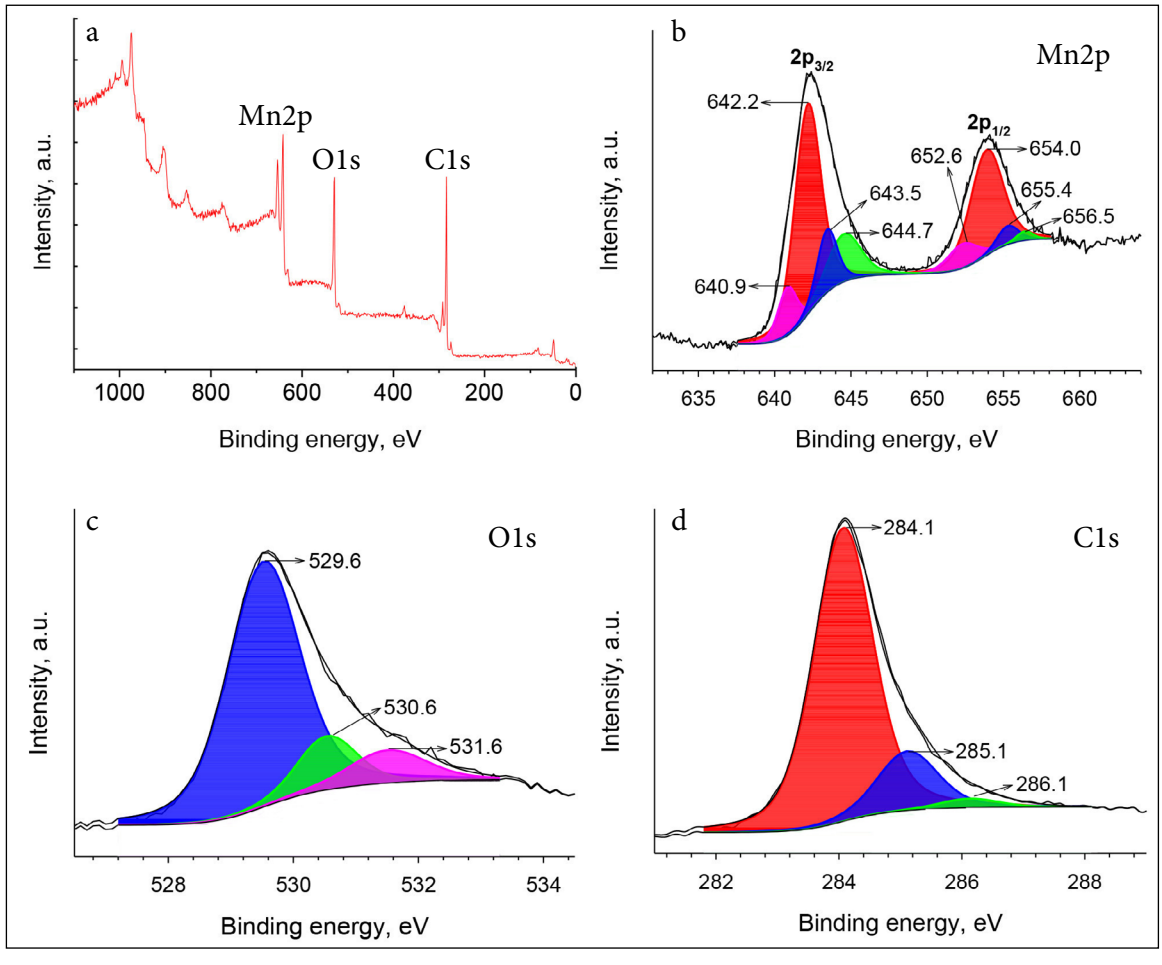

Fig. 3. The survey XPS spectrum (a), Mn 2p (b), O 1s (c) and C 1s (d) for the MnO_2/C-1 sample

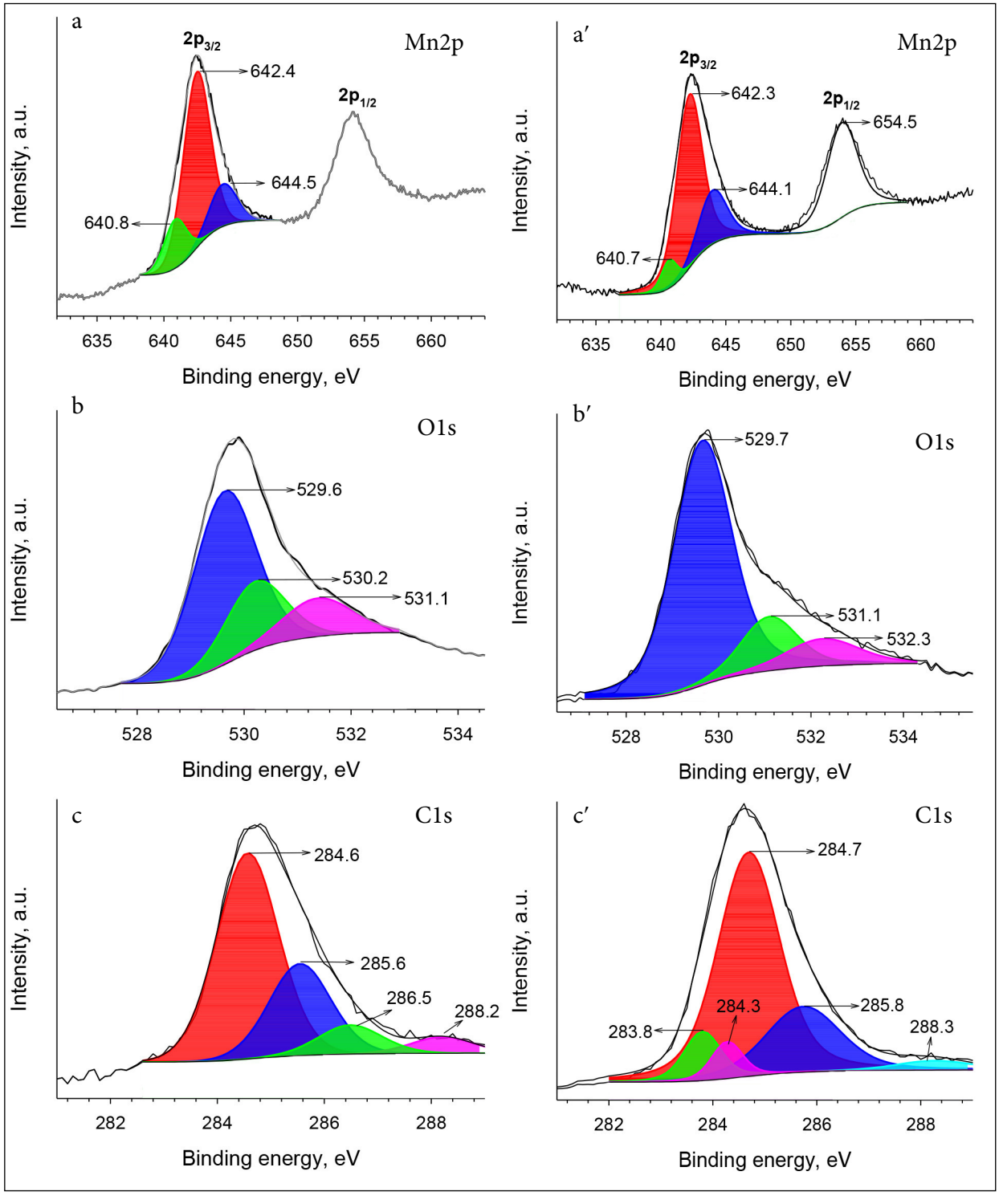

Fig. 4. The XPS spectra of Mn 2p (a, a′), O 1s (b, b′) and C 1s (c, c′) for $MnO_2/C_{CTAB\text{-}1}$ (a, b, c) and $MnO_2/C_{CTAB\text{-}5}$ (a′, b′, c′) samples

in the XPS survey spectrum. It indicates the successful synthesis of MnO_2/C and point to the absence of any other contaminants. Analogous XPS survey spectra were determined for the $MnO_2/C_{CTAB\text{-}1}$ and $MnO_2/C_{CTAB\text{-}5}$ samples, which were prepared using different amounts of CTAB (not presented). The Mn 2p core-level spectrum in Fig. 3b shows a spin-orbit doublet of the main Mn $2p_{3/2}$ and Mn $2p_{1/2}$ peaks located at binding energies (E_b) of 642.33 eV and 654.1 eV, respectively, with a spin-energy separation of 11.77 eV. This value clearly confirms the presence of MnO_2 in the composite [47–49]. Similar spin energy separation values of 11.77 and 11.78 eV with almost

Table 2. **XPS analysis of the elemental composition of MnO_2/C samples prepared by microwave synthesis without CTAB and with CTAB as an additive**

Catalyst	Mn $2p_{3/2}$		O 1s		C 1s	
	E_b, eV	at.%	E_b, eV	at.%	E_b, eV	at.%
MnO_2/C-1	640.9	10.10	529.6	75.58	284.1	80.94
	642.2	58.96	530.6	13.62	285.1	16.59
	643.5	13.64	531.6	10.80	286.1	2.47
	644.7	17.31				
MnO_2/C_{CTAB-1}	640.8	15.84	529.6	61.08	284.6	59.86
	642.4	67.51	530.2	23.70	285.1	26.67
	644.5	16.65	531.1	15.21	286.5	8.66
					288.2	4.81
MnO_2/C_{CTAB-5}	640.7	7.04	529.7	74.00	283.8	8.09
	642.3	69.36	531.1	15.74	284.3	5.16
	644.1	23.61	532.3	10.26	284.7	61.65
					285.8	21.87
					288.3	3.24

the same main Mn $2p_{3/2}$ and Mn $2p_{1/2}$ peaks location at E_b of 642.33 eV and 654.1 eV, and 642.32 eV and 654.1 eV were determined for the prepared MnO_2/C_{CTAB-1} (Fig. 4a) and MnO_2/C_{CTAB-5} (Fig. 4a') nanocomposites, pointing to the existence of MnO_2 in the prepared nanocomposites. Further, the valence of Mn was determined based on the position of the multiple splitting of the Mn 2p peak. For MnO_2/C-1, the Mn $2p_{3/2}$ peak was deconvoluted into four peaks at binding energies of 640.9, 642.2, 643.2 and 644.7 eV, indicating the mixed valence of manganese oxide phases (Fig. 3b). Following the data reported in Refs. [49–52], the position of deconvoluted Mn $2p_{3/2}$ peaks are generally assigned to the Mn (IV) or Mn (II) oxidation state at E_b ranging between 641.85–643.0 eV or 640.10–641.12 eV, respectively. Therefore, the peaks determined at 640.9 and 642.2 eV confirm the presence of Mn(II) and Mn(IV) species in the MnO_2/C-1 sample (Fig. 3b). Moreover, the additional peak at 644.7 eV close to that obtained at 644.9 eV in Refs. [47, 53, 54] could similarly be assigned to a satellite shake-up peak located at higher E_b values than the main component and is a characteristic feature of the MnO phase Mn 2p core peak maximum at 640.7 ± 0.2 eV [55]. Meanwhile, peaks at 643.2 and 644.7 eV based on data in Ref. [54] could be related to Mn (VI and VII) species in the sample. There is no Mn $2p_{3/2}$ signal (647 eV) from permanganate ions, suggesting that permanganate ions have been reduced to MnO_2.

Analogously the Mn $2p_{3/2}$ peaks for the prepared MnO_2/C_{CTAB-1} (Fig. 4a) and MnO_2/C_{CTAB-5} (Fig. 4a') nanocomposites were deconvoluted into three peaks at 640.8, 642.4, and 644.5 and 640.7, 642.3 and 644.1 eV, respectively, and could be assigned to the same Mn oxidation states as mentioned above for the MnO_2/C-1 sample, which was prepared without CTAB. These results apparently indicate the presence of MnO_2 in the mixed valence of manganese oxide phases.

The existence of MnO_2 in the MnO_2/C-1, MnO_2/C_{CTAB-1} and MnO_2/C_{CTAB-5} nanocomposites was further confirmed by the O 1s spectrum, which was deconvoluted into three peaks centered at 529.6, 530.6 and 531.6 eV (Fig. 3b), 529.6, 530.2 and 531.1 eV (Fig. 4b) and 529.7, 531.1 and 532.3 eV (Fig. 4a'), respectively. Usually, the peaks at lower binding energy (529.6–530.6 eV) show the presence of lattice oxygen species (O_α) corresponding to metal–O bonds, whereas the ones at higher E_b of 531.1–532.3 eV correspond to the oxygen chemisorbed by the surface (O_β) [54, 56, 57].

In the case of the MnO_2/C-1 nanocomposite, the high-resolution C 1s spectrum can be deconvoluted into three peaks centered at E_b of 284.1, 285.1 and 286.1 eV (Fig. 3d). The first value could be assigned to the carbon atoms C–C, meanwhile other peaks could be assigned to the oxygen functionalized carbon atoms, such as C–O, or C–OH and C=O [48, 58, 59]. Then, the MnO_2/C

nanocomposites were prepared using CTAB as an additive, additional peaks at 283.8 and 288.3 eV appear in the C 1s spectrum (Fig. 4c, c'). The first E_b peak could be related to the C–M bond [59], while the other one to the OH–C=O or O–C=O bonds [58, 59]. However, it should be taken into account that the carbon signal is quite intense and probably could arise from the organic media, which was used for the synthesis of MnO_2/C samples and which was not completely removed.

It should be noted that the dominating fraction in the prepared MnO_2/C-1, MnO_2/C_{CTAB-1} and MnO_2/C_{CTAB-5} nanocomposites is the MnO_2 phase and is equal to 58.96, 67.51 and 69.36 at.%, respectively (Table 2). At the same time, the MnO (Mn (II)) phase remains significantly lower compared to that determined for the MnO_2 (Mn (IV)) phase (Table 2).

In order to evaluate the electrochemical performance of the MnO_2/C nanocomposites the CV measurements were carried out in a three-electrode system in a 1 M Na_2SO_4 solution within a potential window of 0.05–1.1 V at different scan rates ranging from 10 to 200 mV s^{-1}. Figure 5 shows the CV response of pure carbon (a), MnO_2/C-1 (b) and MnO_2/C-2 (c) that have Mn loadings of 0.140 and 0.239 mg cm^{-2}, respectively. CVs recorded on the $MnO_2/C_{CTAB-0.05}$, $MnO_2/C_{CTAB-0.5}$ and MnO_2/C_{CTAB-5} nanocomposites, that have Mn loadings of 0.207, 0.570 and 1.583 mg cm^{-2}, respectively, are presented in Fig. 5d–f. As evident from the data in Fig. 5a, the CV curves of the pure carbon electrode exhibit a rectangular shape without any deformation even at high scan rates, indicating the ideal double layer capacitor behaviour. With increasing in the scan rate, the current values and, therefore, the integrated areas of CV curves grow up, implying the increase of the specific capacitance. The presence of MnO_2 in the composite that corresponds to Mn loadings of 0.140 (Fig. 5b) or 0.239 (Fig. 5c) mg cm^{-2} still keeps rectangular profiles and mirror symmetry in shape at the same time revealing the weak and broad redox peaks in the CV curves at applied potential scans. They may be ascribed to the fast and reversible Faradaic redox processes of the mixed valence MnO_x, indicating the presence of electrochemical redox reactions during cycling and suggesting the presence of the pseudocapacitive behaviour [2, 51, 61]. The weak and broad redox peaks become more discernable at the MnO_2/C nanocomposites prepared by applying a different amount of CTAB as an additive for synthesis (Fig. 5d–f). The gradual increase in the loading mass of MnO_2 results in the developed current response, indicating a higher amount of active material contributing to the charge storage. Simultaneously a slight deviation for those electrodes from the ideal rectangular shape is observed, especially at higher scan rates. The deviation of CV shapes suggests that a larger amount of Mn loading leads to a thicker layer of the MnO_2 coating and results in a poor conductivity and limited utilization of MnO_2.

Figure 6 represents the summarized current response of the above-mentioned MnO_2/C composites at fixed scan rates of 10 (a) and 200 mV s^{-1} (b). At a higher scan rate of 200 mV s^{-1} the current increases gradually with the increase in the Mn loading in the nanocomposites. This result suggests that more active material contributes to the charge storage. Meanwhile, at a lower scan rate of 10 mV s^{-1} the highest current response is obtained at the MnO_2/C nanocomposite that has the Mn mass loading of 0.570 mg cm^{-2} and was prepared using the CTAB as an additive. Further increase in the Mn mass loading in the nanocomposites reveals the decrease in current, pointing to the existence of some effective critical mass loading of Mn, analogous to the data observed in Ref. [39].

Based on the CV data analysis, the C_s value as a function of scan rate with respect to mass loading was calculated and is plotted in Fig. 7a. Negligible C_s values in a range of 0.979–0.465 F g^{-1} are observed for the pure carbon electrode. Significantly higher values of C_s for the MnO_2/C samples are determined indicating a synergistic effect of carbon that has an excellent electrical conductivity and manganese oxides that have a high specific capacitance. The latter C_s values clearly decrease with the increase in the scan rate, strongly depending on the preparation way of composites. In case if the MnO_2/C samples were prepared without any surfactants and contained mass loading values of 0.140 and 0.239 mg cm^{-2}, the obtained C_s values were equal to 742 and 371 F g^{-1}, respectively, at a scan rate of 10 mV s^{-1} and decreased to 326 and 187 F g^{-1}, respectively, at a scan rate of 200 mV s^{-1}. The MnO_2/C-1 and MnO_2/C-2 nanocomposites preserve 49.3 and 50.4%, respectively, of their

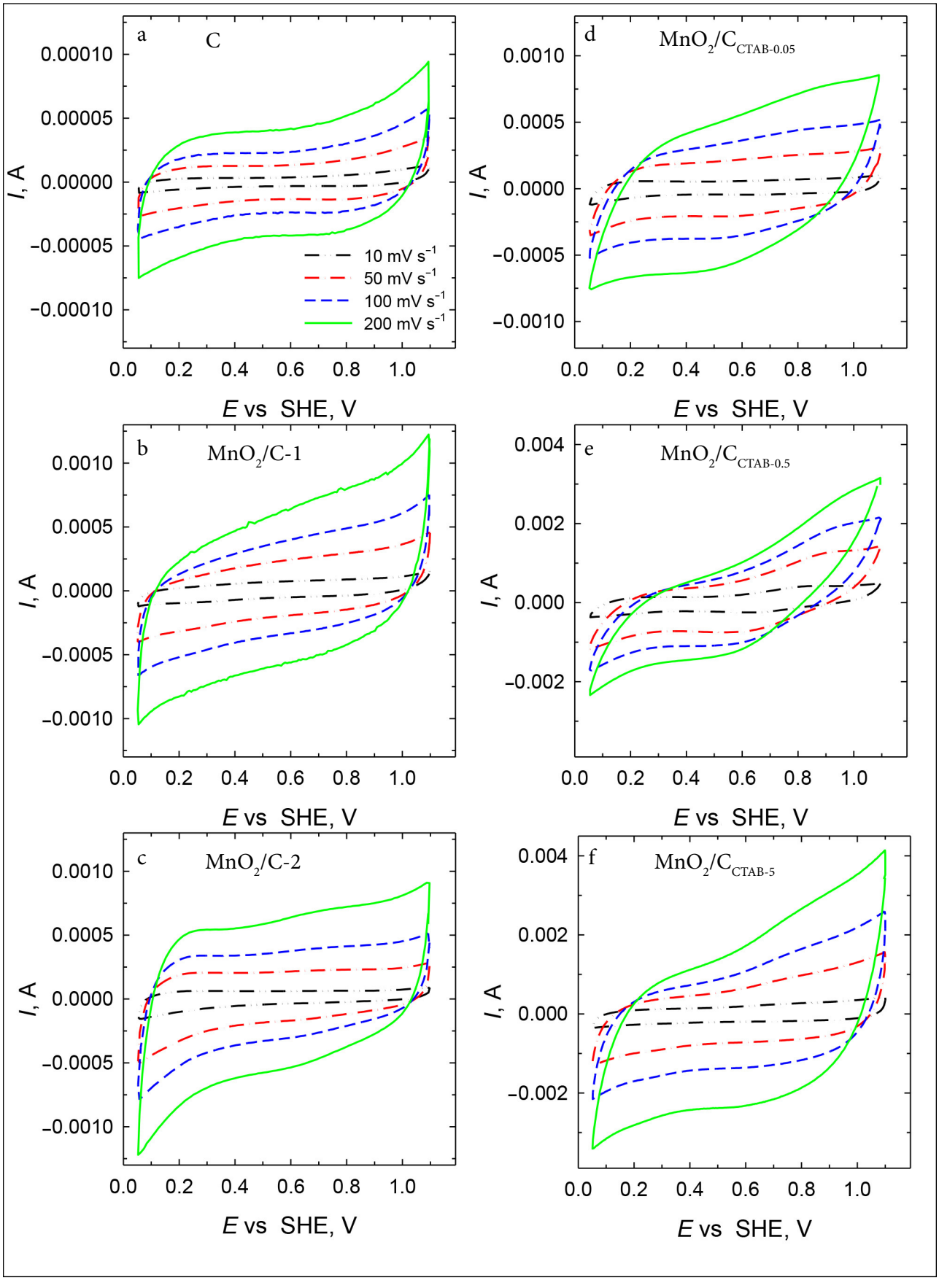

Fig. 5. CVs of C (a), MnO_2/C-1 (b), MnO_2/C-2 (c), $MnO_2/C_{CTAB-0.05}$ (d), $MnO_2/C_{CTAB-0.5}$ (e) and MnO_2/C_{CTAB-5} (f) recorded in 1 M Na_2SO_4 at different scan rates

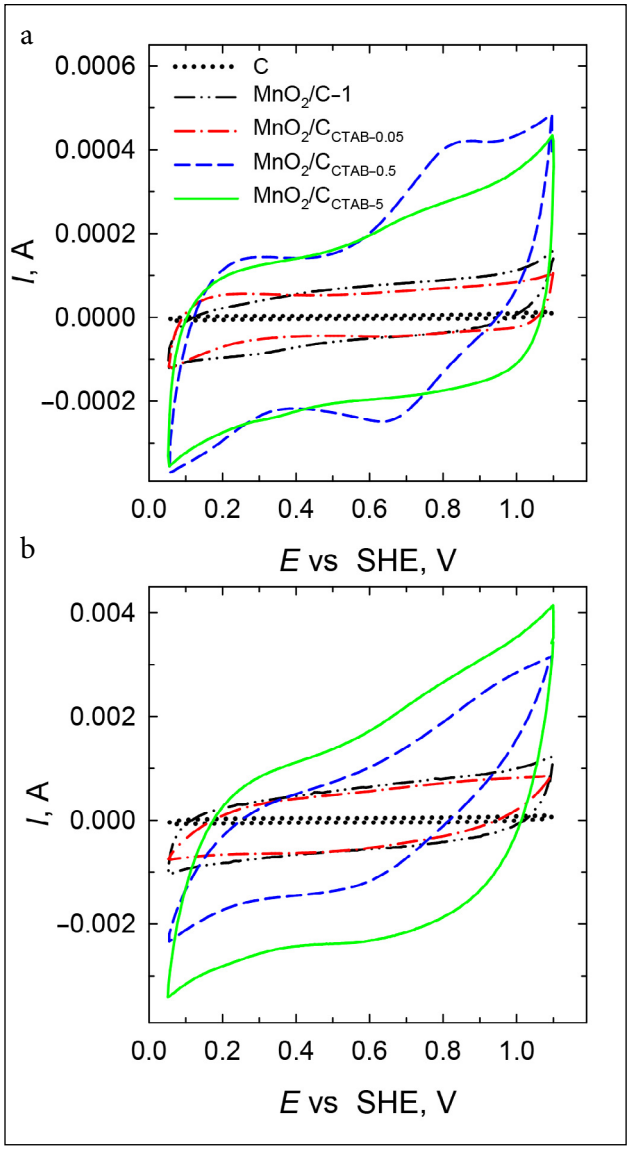

Fig. 6. CVs of C, MnO_2/C-1, $MnO_2/C_{CTAB-0.05}$, $MnO_2/C_{CTAB-0.5}$ and MnO_2/C_{CTAB-5} recorded in 1 M Na_2SO_4 at 10 mV s^{-1} (a) and 200 mV s^{-1} (b)

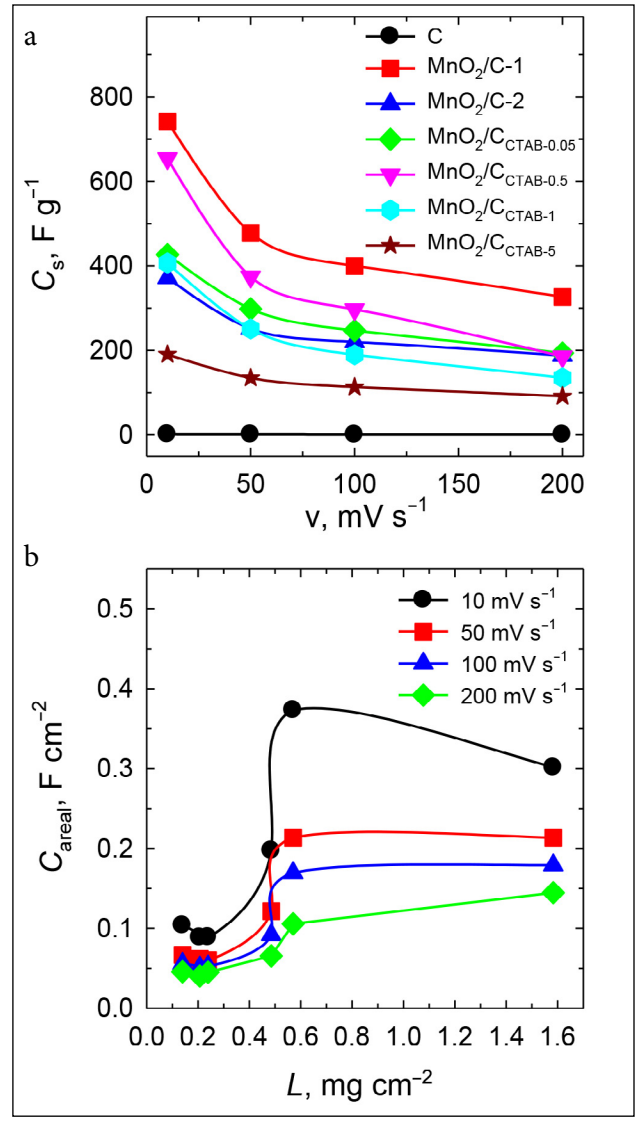

Fig. 7. (a) Specific capacitances of the carbon, MnO_2/C-1, MnO_2/C-2, $MnO_2/C_{CTAB-0.05}$, $MnO_2/C_{CTAB-0.5}$, MnO_2/C_{CTAB-1} and MnO_2/C_{CTAB-5} nanocomposites as a function of scan rate. (b) The areal capacitance versus the loading mass of manganese in the MnO_2/C nanocomposites

specific capacitance (from 742 to 326 F g^{-1} and from 371 to 187 F g^{-1}) as the scan rate increases from 10 to 200 mV s^{-1}.

The increase in mass loading ca. 1.7 times for MnO_2/C-2 resulted in almost the same time decrease of the C_s value, when compared to that determined in the case of MnO_2/C-1. The calculated C_s for the $MnO_2/C_{CTAB-0.05}$, $MnO_2/C_{CTAB-0.5}$, MnO_2/C_{CTAB-1} and MnO_2/C_{CTAB-5} samples that have Mn mass loadings of 0.207, 0.570, 0.485 and 1.583 mg cm^{-2}, respectively, at a scan rate of 10 mV s^{-1} reaches 426, 654, 406 and 190 F g^{-1}. They were obviously higher at a scan rate of 10 mV s^{-1} than those obtained for the MnO_2/C-2 sample prepared in the absence of CTAB and containing the Mn mass loading value of 0.239 mg cm^{-2}, but yielded to that of 0.140 mg cm^{-2} (Fig. 7a). Furthermore, the corresponding specific capacitance of the $MnO_2/C_{CTAB-0.05}$, $MnO_2/C_{CTAB-0.5}$, MnO_2/C_{CTAB-1} and MnO_2/C_{CTAB-5} nanocomposites decays from 426 to 193 F g^{-1}, 654 to 185 F g^{-1}, 406 to 135 F g^{-1}, and 190 to 91 F g^{-1}, respectively, as the scan rate increases from 10 to 200 mV s^{-1}. In addition, 45.3, 28.3, 33.2 and 47.9% of the initial capacitance were maintained at a high scan rate of 200 mV s^{-1} for the $MnO_2/C_{CTAB-0.05}$, $MnO_2/C_{CTAB-0.5}$, MnO_2/C_{CTAB-1} and MnO_2/C_{CTAB-5} samples, respectively.

The use of the CTAB surfactant (on the contrary to the data in literature [23], where increase

in mass loading is mostly related to the decrease in C_s) allowed the increase in mass loading simultaneously demonstrating the increase in C_s, except for the sample that has the highest Mn mass loading of 1.583 mg cm^{-2}. It points to the fact that some optimum concentration of CTAB does exist. Possible explanation could be related not only to the increased amount of the MnO_2 particles in the presence of CTAB, but also to the enhanced and more even dispersion of the MnO_2 particles and the increased specific surface area leading to the increase of the specific capacitance. However, a rather high mass loading of 1.583 mg cm^{-2} (still representing a high enough C_s value of 190 F g^{-1}) possibly could be associated with a too thick MnO_2 layer of limited conductivity. These data are in line with our SEM measurements, demonstrating a large amount of the aggregated nanoparticles in the sample. On the other hand, the superior performance of the composite could be due not only to the presence of the distinguished structure that likely facilitates a free access of electrolyte ions to the electrode surfaces and reduce the diffusion length of the ions and electrons within the electrode phase, but also to the co-existence of mixed valence cations in manganese oxides that benefits the formation of the ionic and electronic defects which could improve the electrochemical properties of the composite as well as to the synergistic effect between the two components of the composite (manganese–carbon), which can also afford facile ion and charge transfer in the electrode [52, 62].

Since areal capacitance plays an important role in commercial applications, the areal capacitance versus the loading mass of manganese derived from CVs was plotted in Fig. 7b. The C_{areal} increased with the increase of loading mass of manganese, indicating that more MnO_2 was contributed to the energy storage. Possibly, it could be attributed to the porous structures of the MnO_2/C composite related to a small resistance and easy electrolyte diffusion. However, C_{areal} increased with the increasing of mass loading until some critical areal mass of MnO_2 was reached at ca. 0.57 mg cm^{-2} (sample MnO_2/$C_{CTAB\text{-}0.5}$). The existence of this critical value might be related to the thickness of MnO_2 close to the Na^+ diffusion length at these scan rates for the MnO_2/C composite. The highest areal capacitance of ca. 0.373 F cm^{-2} was achieved at a slow scan rate of 10 mV s^{-1} with a mass loading of 0.57 mg cm^{-2} and it outperformed those for the sample prepared without a surfactant (Fig. 7b).

Comparison of the supercapacitive behaviour of MnO_2 having different morphology reported in literature and the present work is listed in Table 3, exhibiting a high specific capacitance of our prepared electrode materials.

Table 3. **Comparison of the electrochemical performance for the MnO_2/C electrodes with reported MnO_2-based electrode materials**

Material	Scan rate, mV s^{-1}	Specific capacitance, F g^{-1}	Reference
MnO_2	5	547.0	[63]
MnO_2/CNTs-CNFs	2	374.0	[64]
MnO_2 microtubes	2	152.0	[65]
MnO_2-decorated graphene	5	264.3	[66]
Ultra-long MnO_2 nanowires	2	495.0	[67]
MnO_2/rGO	1	202.5	[68]
MnO_2 nanoparticles	2	298.0	[41]
Amorphous hierarchical porous manganese oxides	1	405.2	[69]
rGO-Mn_3O_4 nanocomposites	5	398.8	[58]
MnO_2 NPs/Ni foam	5	549.0	[70]
MnO_2/MWCNT	2	553.0	[71]
MnO_2/C-1	10	742.0	This study
MnO_2/$C_{CTAB\text{-}0.5}$	10	654.0	This study

CONCLUSIONS

We have successfully synthesized MnO_2/C nanocomposites containing different mass loadings in the presence or absence of the CTAB surfactant by applying the microwave-assisted method. The electrochemical investigations showed a high specific capacitance value of 742 F g^{-1} at a scan rate of 10 mV s^{-1} for the MnO_2/C sample that has been prepared in the absence of the surfactant and contained the Mn mass loading of 0.140 mg cm^{-2}. Meanwhile, the application of CTAB allowed the increase in the mass loading of MnO_2 in the nanocomposites. In the presence of CTAB, the highest value of 654 F g^{-1} at a scan rate of 10 mV s^{-1} has been obtained for MnO_2/C that has the mass loading of 0.570 mg cm^{-2}. It is supposed that the application of CTAB for the MnO_2/C nanocomposite synthesis by the microwave-assisted method plays an important role and allows fabrication of the nanocomposites with enhanced characteristics as electrode materials for supercapacitors application.

ACKNOWLEDGEMENTS

This research is funded by the European Social Fund under Measure No. 09.3.3-LMT-K-712-02-0142 'Development of Competences of Scientists, other Researchers and Students through Practical Research Activities'.

Received 14 November 2019
Accepted 20 November 2019

References

1. Poonam, K. Sharma, A. Arora, S. K. Tripathi, *J. Energy Storage*, **21**, 801 (2019).
2. P. Simon, Y. Gogotsi, *Nat. Mater.*, **7**, 845 (2008).
3. D. P. Dubal, O. Ayyad, V. Ruiz, P. Gómez-Romero, *Chem. Soc. Rev*. **44**, 1777 (2015).
4. J. Jiang, Y. Li, J. Liu, et al., *Adv. Mater.*, **24**, 5166 (2012).
5. C. Yuan, H. B. Wu, Y. Xie, X. W. Lou, *Angew. Chem. Int. Ed.*, **53**, 1488 (2014).
6. C. Liu, F. Li, L.-P. Ma, H.-M. Cheng, *Adv. Mater.*, **22**, E28 (2010).
7. A. Eftekhari, B. Fang, *Int. J. Hydrogen Energy*, **42**, 25143 (2017).
8. X. Zhang, X. Cheng, Q. Zhang, *J. Energy Chem.* **25**, 967 (2016).
9. E. Esther Miller, Y. Hua, F. Handan Tezel, *J. Energy Storage*, **20**, 30 (2018).
10. F. Wang, X. Wu, X. Yuan, et al., *Chem. Soc. Rev.*, **46**, 6816 (2017).
11. C. Liu, X. Yan, F. Hu, et al., *Adv. Mater.*, **30**, 1705713 (2018).
12. W. Guo, C. Yu, S. Li, et al., *Nano Energy*, **57**, 459 (2019).
13. H. El Brouji, O. Briat, J.-M. Vinassa, *Microelectron. Reliab.*, **49**, 1391 (2009).
14. A. Muzaffar, M. Basheer Ahamed, K. Deshmukha, J. Thirumalai, *Renew. Sustain. Energy Rev.*, **101**, 123 (2019).
15. Y. H. Wang, J. R. Zeng, J. Li, et al., *J. Mater. Chem. A*, **3**, 16382 (2015).
16. L. L. Liu, Z. Q. Niu, J. Chen, *Chem. Soc. Rev.*, **45**, 4340 (2016).
17. H. Xia, C. Y. Hong, B. Li, et al., *Adv. Funct. Mater.*, **25**, 627 (2015).
18. A. Afif, S. M. H. Rahman, A. T. Azad, et al., *J. Energy Storage*, **25**, 100852 (2019).
19. X. M. Fan, C. Yu, J. Yang, et al., *Adv. Energy Mater.*, **5**, 1401761 (2015).
20. J. Yang, C. Yu, X. M. Fan, et al., *Adv. Funct. Mater.*, **25**, 2109 (2015).
21. Q. Li, S. Zheng, Y. Xu, et al., *Chem. Engineer. J.*, **333**, 505 (2018).
22. J.-G. Wang, F. Kang, B. Wei, *Prog. Mater. Sci.*, **74**, 51 (2015).
23. M. Huang, F. Li, F. Dong, et al., *J. Mater. Chem. A*, **3**, 21380 (2015).
24. M. Huang, Y. Zhang, F. Li, et al., *Sci. Rep.*, **4**, 3878 (2014).
25. L. Sun, N. Li, S. Zhang, et al., *J. Alloys Compd.*, **789**, 910 (2019).
26. X. Su, L. Yu, G. Cheng, et al., *Appl. Energy*, **153**, 94 (2015).
27. B. Yin, S. Zhang, Y. Jiao, et al., *CrystEngComm.*, **16**, 9999 (2014).
28. R. Lei, H. Zhang, W. Lei, et al., *Mater. Lett.*, **249**, 140 (2019).
29. X. Meng, L. Lu, C. Sun, *ACS Appl. Mater. Interf.*, **10**, 16474 (2018).
30. Y. Qiu, P. Xu, B. Guo, et al., *RSC Adv.*, **4**, 64187 (2014).
31. J. Chu, D. Lu, J. Ma, et al., *Mater. Lett.*, **193**, 263 (2017).
32. H. Cheng, S. Zhao, F. Yi, et al., *J. Alloys Compd.*, **779**, 550 (2019).
33. X. Zhang, X. Meng, S. Gong, et al., *Mater. Lett.*, **179**, 73 (2016).
34. Y. Ping, Z. Liu, J. Li, et al., *J. Alloys Compd.*, **805**, 822 (2019).
35. D.-Y. Feng, Z. Sun, Z.-H. Huang, et al., *J. Power Sources*, **396**, 238 (2018).
36. J. Yang, L. Lian, H. Ruana, et al., *Electrochim. Acta*, **136**, 189 (2014).

37. L. Wang, Y. Zheng, S. Chen, et al., *Electrochim. Acta*, **135**, 380 (2014).
38. H. Zhang, J. Gu, Y. Jiang, et al., *Energy Convers. Manag.*, **86**, 605 (2014).
39. H. Zhang, Y. Wang, C. Liu, H. Jiang, *J. Alloys Compd.*, **517**, 1 (2012).
40. Y. Li, X. Cai, W. Shen, *Electrochim. Acta*, **149**, 306 (2014).
41. M. Aghazadeh, M. R. Ganjali, M. G. Maragheh, *Int. J. Electrochem. Sci.*, **13**, 1161 (2018).
42. X. Zhang, W. Miao, C. Li, et al., *Mater. Research Bull.*, **71**, 111 (2015).
43. S. K. Meher, G. Ranga Rao, *J. Power Sources*, **215**, 317 (2012).
44. X. Zhang, X. Sun, H. Zhang, et al., *Electrochim. Acta*, **87**, 637 (2013).
45. Y. Li, J. Wang, Y. Zhang, M. N. Banis, et al., *J. Colloid Interf. Sci.*, **369**, 123 (2012).
46. H. G. Kang, J. M. Jeong, S. B. Hong, et al., *J. Alloys Compd.*, **770**, 458 (2019).
47. A. A. Audi, P. M. A. Sherwood, *Surf. Interf. Anal.*, **33**, 274 (2002).
48. D. Zhou, H. Lin, F. Zhang, et al., *Electrochim. Acta*, **161**, 427 (2015).
49. A. Ramírez, P. Hillebrand, D. Stellmach, et al., *J. Phys. Chem. C*, **118**, 14073 (2014).
50. A. Moses Ezhil Raj, S. Grace Victoria, V. Bena Jothy, et al., *Appl. Surf. Sci.*, **256**, 2920 (2010).
51. J. Dong, G. Lu, J. Yue, Z. Cheng, X. Kang, *Appl. Surf. Sci.*, **480**, 1116 (2019).
52. Y. Wang, W. Lai, N. Wang, et al., *Energy Environ. Sci.*, **10**, 941 (2017).
53. T. Beyazay, F. E. S. Oztuna, U. Unal, *Electrochim. Acta*, **296**, 916 (2019).
54. M. C. Biesinger, B. P. Payne, A. P. Grosvenor, et al., *Appl. Surf. Sci.*, **257**, 2717 (2011).
55. R. Griss, H. Martinez, S. Cotte, et al., *Appl. Surf. Sci.*, **411**, 449 (2017).
56. W. Yang, Y. Zhua, F. You, et al., *Appl. Catal., B*, **233**, 184 (2018).
57. *X-ray Photoelectron Spectroscopy (XPS) Reference Pages* [https://www.xpsfitting.com].
58. B. S. Singu, R. Yoon, *J. Alloys Compd.*, **770**, 1189 (2019).
59. H. Z. Chi, Y. Q. Wu, Y. K. Shen, et al., *Electrochim. Acta*, **290**, 487 (2018).
60. R. K. Sahoo, A. Das, S. Singh, et al., *Prog. Nat. Sci. Mater. Int.*, **29**, 410 (2019).
61. Y.-T. Weng, H.-A. Pan, R.-C. Lee, et al., *Adv. Energy Mater.*, **5**, 1500772 (2015).
62. J. Zhang, J. Jiang, X. S. Zhao, *J. Phys. Chem. C*, **115**, 6448 (2011).
63. X. Dong, W. Shen, J. Gu, et al., *J. Phys. Chem. B*, **110**, 6015 (2006).
64. J.-G. Wang, Y. Yang, Z.-H. Huang, F. Kang, *Electrochim. Acta*, **75**, 213 (2012).
65. Y. Gao, D. Zheng, X. Xu, et al., *Mater. Lett.*, **204**, 161 (2017).
66. B. S. Singu, K. R. Yoon, *Electrochim. Acta*, **231**, 749 (2017).
67. B. S. Singu, S. E. Hong, K. R. Yoon, *J. Solid State Electrochem.*, **21**, 3215 (2017).
68. Y. Chen, J. Zhang, M. Li, et al., *Electrochim. Acta*, **292**, 115 (2018).
69. Q. Ma, M. Yang, X. Xia, et al., *Electrochim. Acta*, **291**, 9 (2018).
70. T. N. J. I. Edison, R. Atchudan, N. Karthik, D. Xiong, Y. R. Lee, *J. Taiwan Inst. Chem. E.*, **97**, 414 (2019).
71. C. Xue, Y. Hao, Q. Luan, et al., *Electrochim. Acta*, **296**, 94 (2019).

Jolita Jablonskienė, Dijana Šimkūnaitė, Jūratė Vaičiūnienė, Algirdas Selskis, Audrius Drabavičius, Vitalija Jasulaitienė, Loreta Tamašauskaitė-Tamašiūnaitė, Eugenijus Norkus

MnO_2/C NANOKOMPOZITŲ, SUFORMUOTŲ MIKROBANGŲ SINTEZĖS BŪDU DALYVAUJANT PAVIRŠIAUS AKTYVIAJAI MEDŽIAGAI, TAIKYMAS ELEKTROCHEMINIAMS SUPERKONDENSATORIAMS

S a n t r a u k a

MnO_2/C nanokompozitai buvo formuojami taikant mikrobangų sintezę, naudojant skirtingas paviršiaus aktyviosios medžiagos – *cetil timetilamonio bromido* (CTAB) priedo koncentracijas. Suformuotų MnO_2/C nanokompozitų morfologija ir sudėtis buvo tiriami taikant rentgeno fotoelektronų spektroskopiją (XPS), skenuojančiąją elektronų mikroskopiją (FESEM), peršviečiamąją elektroninę mikroskopiją (TEM) ir indukciškai susietos plazmos optinės emisijos spektroskopiją (ICP-OES). MnO_2/C nanokompozitų elektrocheminė elgsena buvo tiriama taikant ciklinę voltamperometriją (CV).

Nustatyta, kad MnO_2/C nanokompozitai, suformuoti nenaudojant CTAB priedo, ir turintys Mn masės įkrovą – 0,140 mg cm^{-2}, pasižymi aukšta specifine talpa (C_s) – 742 F g^{-1}, kuri buvo išmatuota 1 M Na_2SO_4 tirpale, naudojant 10 mV s^{-1} potencialo skleidimo greitį. CTAB priedo naudojimas MnO_2/C nanokompozitų sintezei padidino tiek MnO_2 masės įkrovą nanokompozituose, tiek ir jų C_s. Didžiausia nustatyta MnO_2/C nanokompozitų specifinės talpos vertė buvo lygi 654 F g^{-1}, kai Mn masės įkrova siekė 0,57 mg cm^{-2}, esant elektrodo potencialo skleidimo greičiui 10 mV s^{-1}.